Pitilakis, A.; Seckel, M.; Tasolamprou, A. C.; Liu, F.; Deltsidis, A.; Manessis, D.; Ostmann, A.; Kantartzis, N. V.; Liaskos, C.; Soukoulis, C. M.; Tretyakov, S. A.; Kafesaki, M.; Tsilipakos, O.

Multifunctional Metasurface Architecture for Amplitude, Polarization and Wave-Front Control

Published in:
Physical Review Applied

DOI:
10.1103/PhysRevApplied.17.064060

Published: 01/06/2022

Document Version
Publisher's PDF, also known as Version of record

Please cite the original version:
Pitilakis, A., Seckel, M., Tasolamprou, A. C., Liu, F., Deltsidis, A., Manessis, D., Ostmann, A., Kantartzis, N. V., Liaskos, C., Soukoulis, C. M., Tretyakov, S. A., Kafesaki, M., & Tsilipakos, O. (2022). Multifunctional Metasurface Architecture for Amplitude, Polarization and Wave-Front Control. *Physical Review Applied*, *17*(6), Article 064060. https://doi.org/10.1103/PhysRevApplied.17.064060

Editors' Suggestion

Multifunctional Metasurface Architecture for Amplitude, Polarization and Wave-Front Control

A. Pitilakis,[1,*] M. Seckel,[2] A.C. Tasolamprou,[3] F. Liu,[4,5] A. Deltsidis,[3] D. Manessis,[2] A. Ostmann,[2] N.V. Kantartzis,[1] C. Liaskos,[6] C.M. Soukoulis,[3,7] S.A. Tretyakov,[5] M. Kafesaki,[3,8] and O. Tsilipakos[3,†]

[1] *School of Electrical and Computer Engineering, Aristotle University of Thessaloniki, Thessaloniki GR-54124, Greece*

[2] *System Integration and Interconnection Technologies, Fraunhofer IZM, Berlin 13355, Germany*

[3] *Institute of Electronic Structure and Laser, Foundation for Research and Technology Hellas, Crete, Heraklion GR-70013, Greece*

[4] *Xi'an Jiaotong University, School of Electronic Science and Engineering, Xi'an 710049, China*

[5] *Department of Electronics and Nanoengineering, Aalto University, Aalto FI-00076, Finland*

[6] *Department of Computer Science Engineering, University of Ioannina, Ioannina, Greece*

[7] *Ames Laboratory, U.S. Department of Energy and Department of Physics and Astronomy, Iowa State University, Ames, Iowa 50011, USA*

[8] *Department of Materials Science and Technology, University of Crete, Crete, Heraklion GR-70013, Greece*

(Received 13 January 2022; revised 30 May 2022; accepted 31 May 2022; published 29 June 2022)

Metasurfaces (MSs) have been utilized to manipulate different properties of electromagnetic waves. By combining local control over the wave amplitude, phase, and polarization into a single tunable structure, a multifunctional and reconfigurable metasurface can be realized, capable of full control over incident radiation. Here, we experimentally validate a multifunctional metasurface architecture for the microwave regime, where variable loads are connected behind the back plane to reconfigurably shape the complex surface impedance. As a proof-of-concept step, we fabricate several metasurface instances with static loads in different configurations (surface mount capacitors and resistors of different values in different connection topologies) to validate the approach and showcase the different achievable functionalities. Specifically, we show perfect absorption for oblique incidence (both polarizations), broadband linear-polarization conversion, and beam splitting, demonstrating control over the amplitude, polarization state, and wave front, respectively. Measurements are performed in the 4–18-GHz range inside an anechoic chamber and show good agreement with theoretically anticipated results. Our results clearly demonstrate the practical potential of the proposed architecture for reconfigurable electromagnetic wave manipulation.

DOI: 10.1103/PhysRevApplied.17.064060

I. INTRODUCTION

Metasurfaces, the single-layer version of metamaterials, have attracted considerable interest in recent years [1,2]. They are capable of manipulating the amplitude, phase, and polarization of the incident electromagnetic wave by appropriately engineering the subwavelength resonant building blocks (termed meta-atoms). Maximum functionality can be obtained by combining into a single metasurface the ability to locally control all three aforementioned characteristics [3]. In physical terms, this amounts to locally manipulating the anisotropic complex surface impedance (the real and imaginary parts of the tensor elements) [4]. This approach can lead to multifunctional *and* reconfigurable metasurfaces, which allow for maximum operation versatility [5]. Currently, both static and reconfigurable versions of metasurfaces are being actively researched for a broad range of applications in the microwave and mmWave (5G) frequencies, including absorbers [6], isolators [7,8], filters [9], switchable screens [10], enhanced antennas [11], metasurfaces that can dynamically switch from reflection- to transmission-mode operation [12], and wave-front-shaping devices, which have been both theoretically studied [13] and experimentally demonstrated [14,15].

In Ref. [4], we have conceptualized a metasurface unit cell with a locally and continuously tunable complex surface impedance, for multiple reconfigurable functions. Developing this concept further, in Ref. [16] we have proposed a practical and scalable multifunctional metasurface

*alexpiti@auth.gr
†otsilipakos@iesl.forth.gr

architecture for the microwave regime, where electronic integrated circuits are assembled behind the metasurface back plane in order to dynamically engineer the metasurface properties. The integrated circuits supply tunable resistance and capacitance loads to each meta-atom [17], allowing us to locally shape the complex surface impedance. By cosimulating [16,18] electronic chip and electromagnetic responses, we have theoretically showcased the potential of the proposed structure.

In this work, we report the essential step of experimentally validating the multifunctional metasurface architecture. To this end, we fabricate several instances of the metasurface with static loads mounted behind the back plane in place of the integrated circuits assumed in [16,17]. The fixed surface-mounted devices (SMDs), capacitors and resistors, are placed in different connection topologies for each metasurface instance. This allows us to showcase different functionalities of (i) independent perfect absorption for the two linear polarizations under oblique incidence, (ii) polarization control, illustrated by broadband linear-polarization conversion, and (iii) wave-front manipulation, illustrated by beam splitting. The replacement of the tunable integrated chips with fixed loads serves to experimentally validate the metasurface architecture prior to the costly assembling of the actual chips. Note that the chosen resistance and capacitance values are within the capabilities of the custom chip implementation [16,17], so that the demonstrated functionalities are readily achievable with the reconfigurable version of the proposed multifunctional metasurface.

The remainder of the paper is organized as follows. In Sec. II, we present the metasurface architecture and discuss fabrication and measurement details. Simulation and experimental results are presented in Sec. III for all three showcased functionalities. Finally, the conclusions appear in Sec. IV.

II. MULTIFUNCTIONAL METASURFACE ARCHITECTURE

The multifunctional metasurface under study is a three-metallization-layer printed-circuit-board (PCB) structure based on a high-frequency Panasonic Megtron7N dielectric substrate ($\varepsilon_r = 3.35$, $\tan\delta = 0.002$), the geometry of which is described in Fig. 1. The top metallization layer contains a 2×2 array of square copper patches ($w \times w = 3.95 \times 3.95$ mm) in a symmetric configuration [Fig. 1(a)]; the periodicity is square with lattice constant $a = 9$ mm (approximately $\lambda_0/7$ at the frequency of 5 GHz). The second (middle) metallization layer is the metasurface back plane, so that the structure operates in reflection (negligible transmission). Finally, the third (bottom) metallization layer accommodates the SMD components [Figs. 1(b), 1(d)– 1(f)] or the integrated chip in the reconfigurable version [Fig. 1(c)]. In this way, the loads are "hidden" beneath

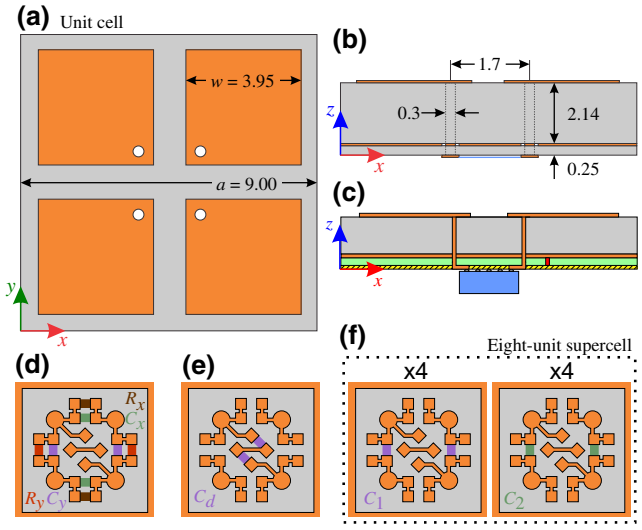

FIG. 1. The architecture of the proposed reconfigurable metasurface: (a) The top view, the unit cell with four patches, and (b) the side view, the three-metallization-layer stack-up (dimensions in millimeters). (c) The reconfigurable version with a chip. (d)–(f) The static load configuration in the bottom metallization layer for: (d) independent perfect absorption for the two linear polarizations—different resistor-capacitor (RC) pairs connect the adjacent patches in the unit cell along the x and y directions; (e) linear-polarization conversion—an appropriate capacitance connects the diagonally adjacent patches in the unit cell; (f) beam splitting—a supercell of unit cells with different capacitances.

the back plane and do not interfere with the incident electromagnetic waves or obstruct the aperture; the connection between the patches and loads is accomplished by means of through vias (TVs). The fabricated [19,20] metasurface boards consist of 18×26 cells, for an effective aperture of 162 mm $\times$ 234 mm. Photographs of both sides of the metasurface boards can be found in Figs. S5(a) and (b) of the Supplemental Material [21].

The four-patch unit-cell geometry along with the possibilities for horizontal, vertical, and diagonal connections behind the back plane is judiciously chosen so as to allow us to electrically bestow anisotropic properties in the surface impedance. Specifically, it provides the ability to address the x and y linear polarization independently (e.g., absorb at different frequencies or incident angles), as well as allow for linear-polarization conversion. The current patterning of the bottom copper layer can accommodate two components in parallel for each of the x and y directions and one series connection in the diagonal branch [Figs. 1(d)–1(f)].

These possibilities offered by our metasurface architecture allow for a broad range of functionalities. By populating the vertical and horizontal SMD slots with appropriate combinations of resistance and capacitance pairs (R_y, C_y and R_x, C_x, respectively), as shown in Fig. 1(d), we can

selectively absorb the two linear polarizations for different frequencies and/or incidence angles. By populating the diagonal branch [Fig. 1(e)], we can couple the two orthogonal linear polarizations and achieve polarization conversion; by using an appropriate capacitance $C_{\text{tot}} = C_d/2$, we can tune the supported resonances and achieve large aggregate spectral bandwidths. Finally, we can form supercells by assembling different components in the constituent unit cells. This is exemplified in Fig. 1(f), where a supercell comprised of eight 9-mm-wide unit cells is formed from two blocks (four unit cells each) with differing capacitance values in the vertical connections (C_1 and C_2, respectively). The supercell dimension exceeds the free-space wavelength, allowing to split the output beam, equivalent to a binary-grating structure. For more details regarding our generic strategy toward multiple functionalities, see Fig. S1 in the Supplemental Material [21].

The fabricated samples are depicted in Fig. 2. They concern three different instances of the metasurface with different SMD components assembled on the back side [Fig. 2(c)] according to the three scenarios depicted in Figs. 1(d)–1(f). For the specific component values in each case, see the caption of Fig. 2. A top view of the fabricated samples, focusing on the four-patch unit cell, is depicted in Fig. 2(a). A corresponding x-ray view is depicted in Fig. 2(b); this inspection is used to verify the electrical continuity between patches, TVs and SMD pads. The metasurface mounted for measurement inside the anechoic chamber is depicted in Fig. 2(d). The assembled boards are mounted on the head of a motorized positioner, allowing for rotation of its mast and head. Standard-gain pyramidal horns are used as transmitting (Tx) and receiving (Rx) antennas; they are mounted either on tripods or on an arm attached on the rotating positioner mast or head [as is the case in Fig. 2(d)], to obtain measurements of the two-dimensional (2D) or three-dimensional scattering patterns. A vector network analyzer (Anritsu 37397D) feeds the horn antennas to perform S-parameter far-field measurements of the metasurface and of a reference reflective plate (of equal dimensions), used for normalization. A photograph of the whole bistatic measurement setup inside the anechoic chamber can be found in Fig. S5(c) of the Supplemental Material [21].

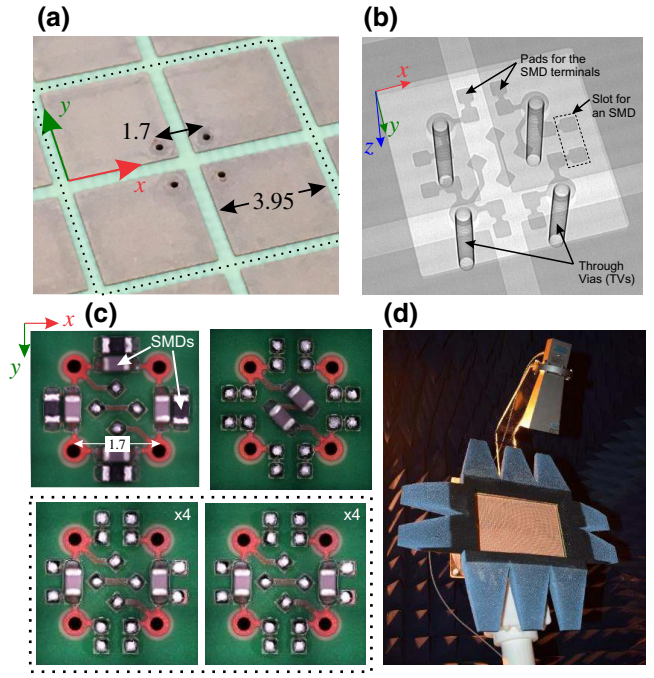

FIG. 2. The fabricated samples and the measurement setup. (a) A photograph of the fabricated sample (top side). (b) An x-ray view verifying the electrical continuity between the patches, through vias and SMD pads. (c) The SMD components assembled on the back side for the three different scenarios schematically depicted in Figs. 1(d)–1(f): top left, $RC_y = 22\ \Omega \parallel 2.7$ pF and $RC_x = 100\ \Omega \parallel 0.8$ pF; top right, $C_d = 0.8$ pF; bottom, $C_1 = 0.8$ pF and $C_2 = 2.7$ pF. (d) The measurement setup inside the anechoic chamber. The metasurface is mounted on the positioner head along with a horn antenna at a fixed angle.

III. EXPERIMENTAL DEMONSTRATION OF MULTIPLE FUNCTIONALITIES

A. Polarization- and direction-sensitive absorber

The first metasurface functionality studied is perfect absorption, where the uniform RC loadings determine the resonance frequency and resonance "depth," primarily governed by the capacitance (C) and resistance (R), respectively. Appropriate RC pairs (SMD components) for two distinct resonances near 5 GHz are assembled on the two parallel x and y slots of each board, as illustrated in Figs. 1(d) and 2(c) (top-left panel). We measure the copolarized reflection spectrum $r = S_{21}$, where a minimum in reflection corresponds to an absorption maximum for our uniform metal-backed metasurface (no transmission and no diffraction orders allowed); note that cross-polarization coupling is negligible for this configuration, as confirmed by both simulation and experiment.

Figure 3(a) depicts results for normal incidence; simulation spectra are obtained through single-cell simulations (periodic boundary conditions) performed in CST Studio; specific details can be found in Sec. S4 of the Supplemental Material [21]. When the electric field is y polarized (x polarized), it is the RC_1 (RC_2) pairs in the vertical(horizontal) slots that govern the resonance. The measurement verifies that the resonance frequencies are to the left and right of 5 GHz in the two cases, as designed; small blue shifts in resonance frequency are attributed to inductive reactance from soldering of the SMD elements, which is more pronounced in the case of the 2.7-pF capacitor (RC_1). Moreover, the measured reflection dips are deeper than those predicted in the simulations, which is attributed to extra losses stemming from parasitic resistance of the

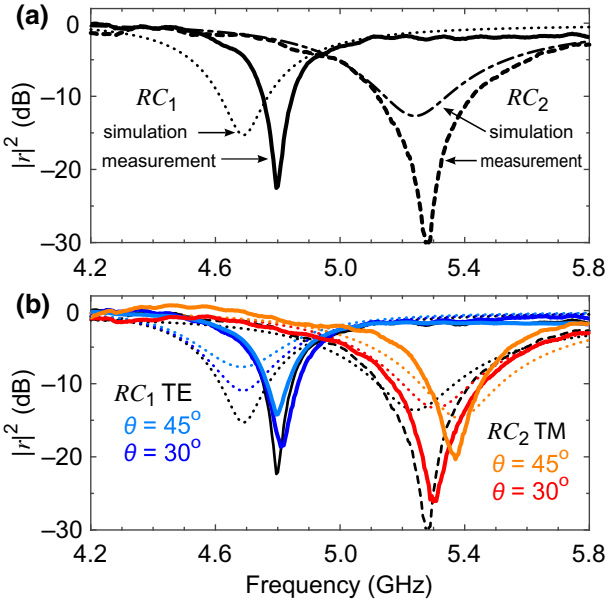

FIG. 3. A comparison of the simulated and measured reflection spectra for the perfect-absorption functionality. The *RC* loads in the vertical and horizontal slots are $RC_1 = 22\ \Omega \parallel 2.7$ pF and $RC_2 = 100\ \Omega \parallel 0.8$ pF, leading to resonances near 4.8 and 5.3 GHz when the electric field is polarized along the y and x axis, respectively. (a) Normal incidence. The resonance frequencies are nicely reproduced in the experiment; the deeper reflection minima in the measurements are due to additional loss compared to the simulation (see text). (b) Oblique incidence inside the x-z plane: TE polarization when $E \parallel y$ involving the RC_1 loads and TM polarization when $E \parallel x$ involving the RC_2 loads. As the incidence angle increases, the TE resonance depth decreases and the TM resonance frequency is blue shifted.

SMD capacitors, soldering, and PCB materials. In anticipation of such additional resistive contributions, the nominal resistance values are chosen such that the metasurface is in the "undercoupled" regime, meaning that any extra resistance will push the operation point toward critical coupling and deepen the reflection minimum [22,23].

It is worth noting that for the case of vertical (horizontal) load connections meant to absorb the E_y (E_x) polarization, the unit cell can be thought of as two identical split-ring resonators (SRRs) vertically sitting in the y-z (x-z) plane [see Sec. S2 and Fig. S2(a) in the Supplemental Material [21]]. The "cut" of the split ring corresponds to the gap between the square patches on the top side of the cell. For this specific configuration (SRR orientation and incidence direction and polarization) shown in the bottom panel of Fig. S2(a), the SRR can be excited both "magnetically" and "electrically" [24] (the electric resonance is typically at higher frequencies than the magnetic). In our case, the resonance that is mediating perfect absorption is of a magnetic nature. This is verified by plotting the surface currents that develop on resonance [see Figs. S2(b) and (c)]. Note that the presence of two SRRs per unit cell serves to effectively increase the density of the resonant loops and, thus, the resonance strength.

Results for oblique incidence inside the x-z plane are depicted in Fig. 3(b). In the case denoted by RC_1 TE (RC_2 TM), the electric field is polarized along the y axis (x axis), leading to TE (TM) polarization. In all cases, the receiver horn is aligned in the specular reflection direction, since the metasurface is uniform and no higher diffraction orders are propagating. In the simulations, we observe that for the TE oblique incidence, as the angle increases, the resonance depth diminishes without a visible frequency shift; the opposite holds for the TM-polarized case: the resonance frequency is visibly shifted (increased) without a change in the resonance depth. These trends are reproduced in the experiment, corroborating the reasonably good agreement between simulation and measurement. A small discrepancy is observed for the TM polarization, where the measured reflection minima become shallower as the incidence angle increases. However, this apparent change concerns small values: from −30 dB to −21 dB. Note that some discrepancy between simulation and measurement is expected, since the simulations refer to the infinitely periodic metasurface, whereas the measurements are conducted with a finite-size metasurface: 18 × 26 cells (162 × 234 mm). This discrepancy will be more pronounced for large incidence angles, since a smaller effective aperture is captured in this case.

B. Broadband polarization converter

The second functionality studied is broadband linear-polarization conversion in reflection by electrically rotating the principal axis of the surface impedance of the metasurface. The metasurface is again loaded uniformly but the loading is placed diagonally inside the square unit cell, as in Fig. 1(e) and the top-right panel of Fig. 2(c), so as to emulate a 45°-cut wire [25] that couples orthogonal (x and y) linear polarizations. We have also assessed the combination of populating one horizontal and one vertical connection in the back of the cell, emulating an "L"-shape geometry, which has been also successfully used for polarization conversion [26], but have found inferior performance compared to the diagonal connection. This time, we only use capacitor loading—i.e., no resistors—to minimize absorption. Following a parametric simulation study, we find that the capacitance value required for broadband and high-amplitude cross-polarized reflection is around 0.5 pF. Since the minimum C value of available commercial SMD components is of the order of 1 pF, we combine two SMD capacitors in series to attain the required value.

Figure 4 presents the simulated and measured cross-polarized reflection (XPR) spectra, under normal incidence. The broadband XPR covering the entire X band (8–12 GHz) arises as a combination of distinct features merging in a continuous aggregate band [27]. In Fig. S4

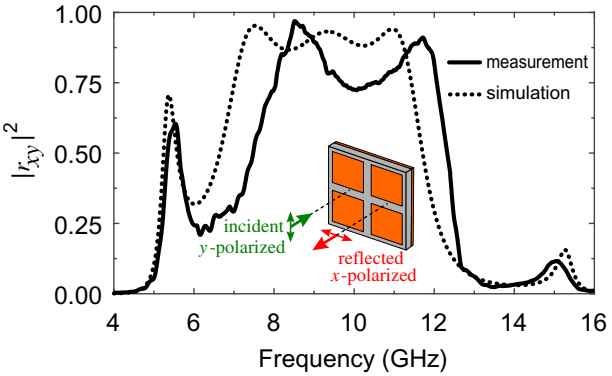

FIG. 4. The simulated and measured cross-polarized reflection spectra under normal incidence for the metasurface with diagonal loading consisting of two 0.8-pF capacitors in series. Note the broad high-amplitude cross-polarized spectrum covering the entire X band (8–12 GHz) and the two isolated peaks near 5.5 and 15 GHz, which are also reproduced in the experiment.

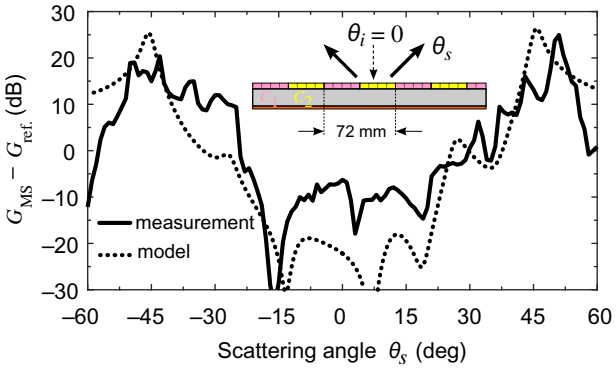

FIG. 5. The semianalytically predicted and measured copolarized scattering gain pattern at 5.3 GHz for a normally illuminated metasurface configured as a binary grating. The grating is inscribed using two reactive loadings (0.8 and 2.7 pF) that exhibit a π phase difference at the specified frequency. The supercell period is $p = 8a = 72$ mm, which results in a two-beam splitting at approximately $\theta_s = \pm 51^\circ$ (± 1 diffraction orders).

of the Supplemental Material [21], we investigate the field profiles of the individual resonances, adopting a simplified metasurface model. The width of the main cross-polarized reflection band is found to be in good agreement between measurement and simulations and approaches approximately 5 GHz. However, the spectral features within the XPR band do not match completely. We attribute this discrepancy to the utilization of several sets of horn antennas (four in total) for covering the frequency ranges 4–6, 6–8, 8–12, and 12–18 GHz (approximately), in order to perform this wide-band measurement. The four measurements are subsequently stitched together to end up with the result depicted in Fig. 4. In particular, the peaks near the edges of each measurement may be somewhat distorted. We think that this is the case with the first and second peaks, which are close to the stitching (horn swapping) at 8.2 GHz. This hypothesis is corroborated by the fact that the outlying peaks near 5.5 and 15 GHz show excellent agreement between simulation and measurement. Finally, we note that for oblique incidence, the bandwidth of XPR deteriorates; for angles above 15°, two reflection dips slice the XPR spectrum into three bands, as can be seen in Fig. S6 of the Supplemental Material [21].

C. Wave-front shaping

The last functionality studied is wave-front manipulation, exemplified through the case of beam splitting: A normally incident beam (plane wave) is divided into two approximately equal beams in symmetric oblique directions, i.e., $\pm\theta_s$. This is accomplished by applying a (nonuniform) binary encoding across the aperture, as shown in Fig. 1(f) and the bottom panel of Fig. 2(c). Specifically, we identify two different capacitor load values, which lead to reflection coefficients that exhibit a near-unity amplitude and a 180° phase difference at the operating frequency; for details, see Sec. S7 in the Supplemental Material [21]. For our unit-cell design and target band of 4–6 GHz, the two required capacitance values are in the vicinity of 1 and 3 pF, respectively. Subsequently, we assemble these loads so as to form supercells, the extent of which is larger than the wavelength ($\lambda < p < 2\lambda$, p is the supercell period), and we implement a flat binary grating on the metasurface (a "stripes" pattern), which leads to first-order diffraction modes (scattered beams) in directions $\theta_s = \pm\sin^{-1}\{\lambda/p\}$, assuming normal incidence and an infinite aperture. In our case, we opt for a period of $p = 8a = 72$ mm, made from eight 9-mm-wide unit cells arranged in four columns of cells with $C_1 = 0.8$ pF loading followed by four columns of cells with $C_2 = 2.7$ pF loading; each cell contains two identical SMD capacitors placed in the vertical slots, as shown in Fig. 1(f) and the bottom panel of Fig. 2(c). When the illuminating field is polarized parallel to these loads, the infinite grating produces diffraction lobes approximately in the $\theta_s = \pm 51^\circ$ directions; longer periods lead to diffraction closer to specular reflection (normal, in our case) but cannot be accommodated well inside our finite metasurface.

The measured and semianalytically extracted 2D scattering patterns, depicted as the metasurface gain normalized to the reference reflector (of same aperture), are illustrated in Fig. 5, showing good agreement overall, despite some degradation near the splitting maxima. In this case, the theoretical results are not from full-wave simulations but are based on the Huygens-Fresnel principle [28], which estimates the scattered far-field pattern from the unit-cell reflection coefficients using Fraunhofer-diffraction superposition; implementation details for modeling the metasurface and the absorbing-foam frame seen in

Fig. 2(d) can be found in Sec. S8 of the Supplemental Material [21]. The asymmetry in the scattering pattern with respect to the "right" and "left" lobes is due to the incommensurate number of cells between the metasurface aperture (26) and the grating period (eight), in combination with the partially reflecting material that frames the effective aperture [Fig. 2(d)]; more details can be found in the Supplemental Material [21]. This is also the cause of the split-lobe maxima appearing at slightly different angles than the prescribed ($\theta_s = \pm 51^\circ$) in simulation and measurement.

Finally, we note that the very same structure can be used for beam steering or anomalous reflection, as outlined in Fig. S11 of the Supplemental Material [21].

IV. CONCLUSIONS

In conclusion, with this family of static-load metasurfaces, we experimentally verify our approach toward a microwave multifunctional *and* reconfigurable metasurface. The simulation and experimental results demonstrate successful control of the amplitude, wave front, and polarization. The capability to arbitrarily engineer the anisotropic complex surface conductivity of our proposed metasurface also makes it a promising candidate for functionalities with strong angular asymmetry [29,30].

More generally, this study serves as a proof of concept for the broader software-controlled intelligent metasurface vision, i.e., when the resistive *and* capacitive loads are supplied by chips embedded in the unit cells, forming an interconnected controller network that is computer controlled [3]. The measured performance using commercial-off-the-shelf (COTS) SMD loads exceeds our expectations, particularly for the demanding absorber functionality; consequently, we anticipate similar or improved in-band performance when using custom-designed chips instead of COTS components. Note that the embedding of such chips in the back side of the unit cells [16,17] will not disturb the electromagnetic performance of the metasurface, owing to the decoupling offered by the back plane; nor will it obstruct its aperture.

The proposed architecture, originally targeted for operation in reflection, can in principle be used for operation in transmission as well. To this end, the uniform metallic back plane, i.e., the middle metallization layer in Figs. 1(b), and 1(c), would have to be restructured to allow for transmission through the structure. Note that the middle (or bottom) metallization layer would still need to include some metallic features in order to engineer the magnetic response of the structure; the proper combination of electric and magnetic responses allows for either forward or backward unidirectional scattering, as exemplified by Huygens [31] and "antimatched" [27] metasurfaces, respectively.

ACKNOWLEDGMENTS

This work was supported by the European Union Horizon 2020 Research and Innovation Programme—Future Emerging Topics (FET Open) under Grants No. 736876 (project VISORSURF, "A Hypervisor for Metasurface Functionalities") and No. 829061 (project NANOPOLY, "High-Performance Electronic Components Based on Metamaterials"); by the European Union and Greek national funds through the Operational Program Competitiveness, Entrepreneurship and Innovation, under the call "Research–Create–Innovate" (Project Code No. T1EDK-02784); and by the Hellenic Foundation for Research and Innovation (HFRI) under the "2nd Call for HFRI Research Projects to Support Post-Doctoral Researchers" (Project No. 916, PHOTOSURF, "Novel Multiresonant Photonic Metasurfaces for Broadband Control of Light"). We acknowledge Professor Julius Georgiou for insights on the compatibility of cell designs with custom-made controllable chips as cell loads, Dr. Georgios Pyrialakos and Dr. Michail Christodoulou for the anechoic chamber setup, and the entire VISORSURF Project Consortium for useful discussions.

[1] S. B. Glybovski, S. A. Tretyakov, P. A. Belov, Y. S. Kivshar, and C. R. Simovski, Metasurfaces: From microwaves to visible, Phys. Rep. **634**, 1 (2016).

[2] Q. He, S. Sun, and L. Zhou, Tunable/reconfigurable metasurfaces: Physics and applications, Research **2019**, 1 (2019).

[3] O. Tsilipakos *et al.*, Toward intelligent metasurfaces: The progress from globally tunable metasurfaces to software-defined metasurfaces with an embedded network of controllers, Adv. Opt. Mater. **8**, 2000783 (2020).

[4] F. Liu, O. Tsilipakos, A. Pitilakis, A. C. Tasolamprou, M. S. Mirmoosa, N. V. Kantartzis, D.-H. Kwon, M. Kafesaki, C. M. Soukoulis, and S. A. Tretyakov, Intelligent Metasurfaces with Continuously Tunable Local Surface Impedance for Multiple Reconfigurable Functions, Phys. Rev. Appl. **11**, 044024 (2019).

[5] A. Pitilakis, A. C. Tasolamprou, C. Liaskos, F. Liu, O. Tsilipakos, X. Wang, M. S. Mirmoosa, K. Kossifos, J. Georgiou, A. Pitsilides, N. Kantartzis, S. Ioannidis, E. N. Economou, M. Kafesaki, S. A. Tretyakov, and C. M. Soukoulis, in *2018 12th International Congress on Artificial Materials for Novel Wave Phenomena (Metamaterials)* (IEEE, Helsinki, Finland, 2018).

[6] S. D. Assimonis and V. Fusco, Polarization insensitive, wide-angle, ultra-wideband, flexible, resistively loaded, electromagnetic metamaterial absorber using conventional inkjet-printing technology, Sci. Rep. **9**, 12334 (2019).

[7] D. Ramaccia, D. L. Sounas, A. V. Marini, A. Toscano, and F. Bilotti, Electromagnetic isolation induced by time-varying metasurfaces: Nonreciprocal bragg grating, IEEE Antennas Wirel. Propag. Lett. **19**, 1886 (2020).

[8] S. Taravati and G. V. Eleftheriades, Full-Duplex Nonreciprocal Beam Steering by Time-Modulated Phase-Gradient Metasurfaces, Phys. Rev. Appl. **14**, 014027 (2020).

[9] I.-J. Hwang, D.-J. Yun, J.-I. Park, Y.-P. Hong, and I.-H. Lee, Design of dual-band single-layer metasurfaces for millimeter-wave 5G communication systems, Appl. Phys. Lett. **119**, 174101 (2021).

[10] A. de Lustrac, B. Ratni, G.-P. Piau, Y. Duval, and S. N. Burokur, Tri-state metasurface-based electromagnetic screen with switchable reflection, transmission, and absorption functionalities, ACS Appl. Electron. Mater. **3**, 1184 (2021).

[11] D. R. Smith, O. Yurduseven, L. P. Mancera, P. Bowen, and N. B. Kundtz, Analysis of a Waveguide-Fed Metasurface Antenna, Phys. Rev. Appl. **8**, 054048 (2017).

[12] H. L. Wang, H. F. Ma, M. Chen, S. Sun, and T. J. Cui, A reconfigurable multifunctional metasurface for full-space control of electromagnetic waves, Adv. Funct. Mater. **31**, 2100275 (2021).

[13] O. Yurduseven, S. D. Assimonis, and M. Matthaiou, Intelligent reflecting surfaces with spatial modulation: An electromagnetic perspective, IEEE Open J. Commun. Soc. **1**, 1256 (2020).

[14] T. Cai, G. Wang, S. Tang, H. Xu, J. Duan, H. Guo, F. Guan, S. Sun, Q. He, and L. Zhou, High-Efficiency and Full-Space Manipulation of Electromagnetic Wave Fronts with Metasurfaces, Phys. Rev. Appl. **8**, 034033 (2017).

[15] R. Feng, B. Ratni, J. Yi, H. Zhang, A. de Lustrac, and S. N. Burokur, in *2021 15th European Conference on Antennas and Propagation (EuCAP)* (IEEE, 2021).

[16] A. Pitilakis, O. Tsilipakos, F. Liu, K. M. Kossifos, A. C. Tasolamprou, D.-H. Kwon, M. S. Mirmoosa, D. Manessis, N. V. Kantartzis, C. Liaskos, M. A. Antoniades, J. Georgiou, C. M. Soukoulis, M. Kafesaki, and S. A. Tretyakov, A multi-functional reconfigurable metasurface: Electromagnetic design accounting for fabrication aspects, IEEE Trans. Antennas Propag. **69**, 1440 (2021).

[17] K. M. Kossifos, L. Petrou, G. Varnava, A. Pitilakis, O. Tsilipakos, F. Liu, P. Karousios, A. C. Tasolamprou, M. Seckel, D. Manessis, N. V. Kantartzis, D.-H. Kwon, M. A. Antoniades, and J. Georgiou, Toward the realization of a programmable metasurface absorber enabled by custom integrated circuit technology, IEEE Access **8**, 92986 (2020).

[18] S. Koziel and A. Pietrenko-Dabrowska, On geometry parameterization for simulation-driven design closure of antenna structures, Sci. Rep. **11**, 24304 (2021).

[19] D. Manessis, M. Seckel, L. Fu, O. Tsilipakos, A. Pitilakis, A. Tasolamprou, K. Kossifos, G. Varnava, C. Liaskos, M. Kafesaki, C. M. Soukoulis, S. Tretyakov, J. Georgiou, A. Ostmann, R. Aschenbrenner, M. Schneider-Ramelow, and K.-D. Lang, in *2020 IEEE 8th Electronics System-Integration Technology Conference (ESTC)* (IEEE, Tonsberg, Norway, 2020).

[20] D. Manessis, S. Kosmider, L. Boettcher, M. Seckel, K. Murugesan, U. Maas, I. Ndip, A. Ostmann, R. Aschenbrenner, M. Schneider-Ramelow, and K.-D. Lang, in *2021 23rd European Microelectronics and Packaging Conference & Exhibition (EMPC)* (IEEE, 2021).

[21] See the Supplemental Material at http://link.aps.org/supplemental/10.1103/PhysRevApplied.17.064060 for (i) the conceptual strategy for multifunctionality, (ii) the nature of the supported resonance leading to perfect absorption, (iii) a simplified model and the underlying resonances of the polarization-conversion functionality, (iv) implementation details for full-wave simulation at the unit-cell level, (v) additional photographs of the fabricated samples and the measurement setup, (vi) the cross-polarization response for oblique incidence, (vii) the unit-cell states for the beam-splitting functionality, and (viii) details of the Huygens-Fresnel methodology for obtaining the far-field radiation pattern.

[22] X. Zhang, Q. Li, F. Liu, M. Qiu, S. Sun, Q. He, and L. Zhou, Controlling angular dispersions in optical metasurfaces, Light: Sci. Appl. **9**, 76 (2020).

[23] T. Christopoulos, O. Tsilipakos, G. Sinatkas, and E. E. Kriezis, On the calculation of the quality factor in contemporary photonic resonant structures, Opt. Express **27**, 14505 (2019).

[24] M. Kafesaki, T. Koschny, R. S. Penciu, T. F. Gundogdu, E. N. Economou, and C. M. Soukoulis, Left-handed metamaterials: Detailed numerical studies of the transmission properties, J. Opt. A: Pure Appl. Opt. **7**, S12 (2005).

[25] N. K. Grady, J. E. Heyes, D. R. Chowdhury, Y. Zeng, M. T. Reiten, A. K. Azad, A. J. Taylor, D. A. R. Dalvit, and H. T. Chen, Terahertz metamaterials for linear polarization conversion and anomalous refraction, Science **304**, 1304 (2013).

[26] Q. Lévesque, M. Makhsiyan, P. Bouchon, F. Pardo, J. Jaeck, N. Bardou, C. Dupuis, R. Haïdar, and J.-L. Pelouard, Plasmonic planar antenna for wideband and efficient linear polarization conversion, Appl. Phys. Lett. **104**, 111105 (2014).

[27] O. Tsilipakos, L. Zhang, M. Kafesaki, C. M. Soukoulis, and T. Koschny, Experimental implementation of achromatic multiresonant metasurface for broadband pulse delay, ACS Photonics **8**, 1649 (2021).

[28] H. Taghvaee, S. Abadal, A. Pitilakis, O. Tsilipakos, A. C. Tasolamprou, C. Liaskos, M. Kafesaki, N. V. Kantartzis, A. Cabellos-Aparicio, and E. Alarcon, Scalability analysis of programmable metasurfaces for beam steering, IEEE Access **8**, 105320 (2020).

[29] H. Fan, J. Li, Y. Lai, and J. Luo, Optical Brewster Metasurfaces Exhibiting Ultrabroadband Reflectionless Absorption and Extreme Angular Asymmetry, Phys. Rev. Appl. **16**, 044064 (2021).

[30] X. Wang, A. Díaz-Rubio, V. S. Asadchy, G. Ptitcyn, A. A. Generalov, J. Ala-Laurinaho, and S. A. Tretyakov, Extreme Asymmetry in Metasurfaces via Evanescent Fields Engineering: Angular-Asymmetric Absorption, Phys. Rev. Lett. **121**, 256802 (2018).

[31] C. Pfeiffer and A. Grbic, Metamaterial Huygens' Surfaces: Tailoring Wave Fronts with Reflectionless Sheets, Phys. Rev. Lett. **110**, 197401 (2013).